Single- and cross-channel nonlinear interference in the Gaussian Noise model with rectangular spectra

Alberto Bononi,[1,*] **Ottmar Beucher,**[2] **and Paolo Serena**[1]

[1]*Dip. Ing. Inf., Università degli Studi di Parma, Parma, Italy*
[2]*Fakultät Maschinenbau und Mechatronik, Hochschule Karlsruhe - Technik und Wirtschaft, Karlsruhe, Germany*

[*]*alberto.bononi@unipr.it*

Abstract: New semi-analytic formulas of the power spectral density (PSD) of single- and cross-channel nonlinear interference (NLI) in coherent optical links for which the Gaussian Noise (GN) model applies are presented. From the PSD, a new bound on cross-channel NLI power is obtained. The new formulas are useful to both quickly compute single- and cross-channel NLI power, and to test the accuracy of numerical routines that directly solve the double frequency integral in the GN reference formula.

References and links

1. A. Carena, V. Curri, G. Bosco, P. Poggiolini, and F. Forghieri, "Modeling of the impact of non-linear propagation effects in uncompensated optical coherent transmission links," J. Lightwave Technol. **30**(10), 1524–1539 (2012).
2. P. Poggiolini, "The GN model of non-linear propagation in uncompensated coherent optical systems," J. Lightwave Technol. **30**(24), 3857–3879 (2012).
3. S. Savory, "Approximations for the nonlinear self-channel interference of channels with rectangular spectra," IEEE Photonics Technol. Lett. **25**(10), 961–964 (2013).
4. V. Curri, A. Carena, P. Poggiolini, G. Bosco, and F. Forghieri, "Extension and validation of the GN model for non-linear interference to uncompensated links using Raman amplification," Opt. Express **21**(3), 3308–3317 (2013).
5. P. Johannisson and M. Karlsson, "Perturbation analysis of nonlinear propagation in a strongly dispersive optical communication system," J. Lightwave Technol. **31**(8), 1273–1282 (2013).
6. A. Bononi and P. Serena, "An alternative derivation of Johannisson's regular perturbation model," arXiv:1207.4729v1 [physics.optics] (2012).
7. P. Serena and A. Bononi, "On the accuracy of the Gaussian nonlinear model for dispersion-unmanaged coherent links," in *Proc. ECOC'13* (2013), paper Th1D3.
8. R. Dar, M. Feder, A. Mecozzi, and M. Shtaif, "Properties of nonlinear noise in long, dispersion-uncompensated fiber links," Opt. Express **21**(22), 25685–25699 (2013).
9. P. Serena and A. Bononi, "An alternative approach to the Gaussian noise model and its system implications," J. Lightwave Technol. **31**(22), 3489–3499 (2013).
10. M. Nazarathy, J. Khurgin, R. Weidenfeld, Y. Meiman, P. Cho, R. Noe, I. Shpantzer, and V. Karagodsky, "Phased-array cancellation of nonlinear FWM in coherent OFDM dispersive multi-span links," Opt. Express **16**(20), 15777–15810 (2008).
11. A. Bononi, P. Serena, N. Rossi, E. Grellier, and F. Vacondio, "Modeling nonlinearity in coherent transmissions with dominant intrachannel-four-wave-mixing," Opt. Express **20**(7), 7777–7791 (2012).
12. X. Chen and W. Shieh, "Closed-form expressions for nonlinear transmission performance of densely spaced coherent optical OFDM systems," Opt. Express **18**(18), 19039–19054 (2010).
13. A. Bononi and O. Beucher, "Semi-analytic formulas of single-channel and cross-channel nonlinear interference in highly-dispersed WDM coherent optical links with rectangular signal spectra," arXiv:1309.0244v1 [physics.optics] (2013).

14. A. V. Oppenheim and R. W. Schafer, *Discrete-Time Signal Processing* (Prenctice-Hall, 1989).
15. "Optilux Toolbox," http://www.optilux.sourceforge.net.
16. A. Bononi, N. Rossi, and P. Serena, "Transmission limitations due to fiber nonlinearity," in *Proc. OFC'11* (2011), paper OWO7.
17. E. Grellier and A. Bononi, "Quality parameter for coherent transmissions with Gaussian-distributed nonlinear noise," Opt. Express **19**(13), 12781–12788 (2011).
18. A. Bononi, N. Rossi, and P. Serena, "On the nonlinear threshold versus distance in long-haul highly-dispersive coherent systems," Opt. Express **20**, B204–B216 (2012).
19. A. Mecozzi and R. J. Essiambre, "Nonlinear Shannon limit in pseudolinear coherent systems," J. Lightwave Technol. **30**(12), 2011–2024 (2012),
20. O. Rival and K. Mheidly, "Accumulation rate of inter and intra-channel nonlinear distortions in uncompensated 100G PDM-QPSK systems," in *Proc. OFC'12* (2012), paper JW2A.52.
21. X. Wei, "Power-weighted dispersion distribution function for characterizing nonlinear properties of long-haul optical transmission links," Opt. Lett. **31**(17) 2544–2546 (2006).
22. B. Châtelain, C. Laperle, K. Roberts, M. Chagnon, X. Xu, A. Borowiec, F. Gagnon, and D. V. Plant, "A family of Nyquist pulses for coherent optical communications," Opt. Express **20**, 8397–8416 (2012).
23. J. G. Proakis and M. Salehi, *Communication Systems Engineering*, 2nd ed. (Prentice-Hall, 2002).
24. P. Poggiolini, A. Carena, V. Curri, G. Bosco, and F. Forghieri, "Analytical modeling of non-linear propagation in uncompensated optical transmission links," IEEE Photonics Technol. Lett. **23**, 742–744 (2011).

1. Introduction

The Gaussian Noise (GN) model has recently been shown to effectively predict the system performance of highly-dispersed coherent optical transmission systems, such as high baud-rate dispersion-uncompensated (DU) systems [1, 2]. In such a model, the GN reference formula (GNRF) provides a formally elegant and compact expression of the power spectral density (PSD) of the received nonlinear interference (NLI). However, the GNRF involves a double frequency integration which poses non-trivial numerical problems for multi-span wavelength division multiplexed (WDM) systems. Many of the numerical integration issues have been already addressed in [2]. Given the practical importance of developing an accurate GNRF numerical evaluator, however, for accuracy testing it proves quite useful to have exact expressions of the NLI PSD in special realistic cases. The case of rectangular per-channel input spectra has already served to clarify the integration regions and derive closed-form 'asinh' NLI PSD approximations [2], and to obtain improved expressions of received NLI power in the single-channel/Nyquist-WDM case [3].

In this paper, we derive new *exact* single-integral expressions of the NLI PSD in the GNRF for both Nyquist and non-Nyquist WDM systems with input rectangular per-channel spectra. We provide explicit PSD formulas for both the single-channel interference (SCI) and the cross-channel interference (XCI) [2]. We formulate the GNRF in a generalized form that applies to any link configuration, be it with concentrated or distributed amplification, with or without in-line compensation, and with possibly different spans. All link details are summarized by the *kernel* frequency function [4–6]. We verify the derived NLI PSD formulas for rectangular input spectra against split-step Fourier (SSF) simulations performed according to the key assumptions of the GNRF, i.e., that every input WDM channel is a low-power complex Gaussian process [6]. A discussion of how closely the GNRF approximates the NLI with digital input signals and specific modulation formats is beyond the scope of this paper, and is the topic of on-going investigations [7, 8]. Having verified that NLI PSDs are consistent with SSF simulations, we next study how SCI and XCI power scales with number of channels, number of spans, dispersion, signal bandwidth and frequency spacing, so that we can easily discriminate the dominant nonlinear effect. We finally derive a new upper-bound (UB) to the XCI power and check its accuracy.

The paper is organized as follows. Sec. 2 summarizes the needed background on the GNRF,

and introduces the change of integration variables that leads to the new NLI PSD expressions for rectangular input spectra. Sec. 3 tackles the single-channel and Nyquist-WDM cases and also discusses the over-estimation when using the zero-frequency value of the NLI PSD to get the NLI power. Sec. 4 tackles the non-Nyquist XCI NLI and derives the new UB to the XCI power. Sec. 5 contains numerical examples of NLI scaling with major system parameters. Sec. 6 summarizes the main findings of the paper.

2. The GN reference formula

In dual-polarization transmission with uncorrelated signals with identical spectra on the two polarizations, the GNRF yields the NLI PSD as $G_{NLI}(f) = \frac{16}{27}I(f)$, with [1, 2, 5, 6]:

$$I(f) \triangleq \iint\limits_{-\infty}^{\infty} |\mathcal{K}(f_1 f_2)|^2 G(f+f_1) G(f+f_2) G(f+f_1+f_2) \mathrm{d}f_1 \mathrm{d}f_2 \qquad (1)$$

where $G(f)$ is the PSD of the complex signal field at system input, and the scalar *kernel* when higher-order dispersion is neglected is [5, 6]:

$$\mathcal{K}(v) \triangleq \int_0^L \gamma(s)\mathcal{G}(s)\mathrm{e}^{-j(2\pi)^2 C(s)v}\mathrm{d}s \qquad (2)$$

where L is total system length, $\gamma(z)$ the fiber nonlinear coefficient, $\mathcal{G}(s)$ the power gain from 0 to s, and $C(s) \triangleq C_0 - \int_0^s \beta_2(s')\mathrm{d}s'$ the cumulated dispersion from 0 to s, with β_2 the dispersion parameter and C_0 the pre-compensation; C has here the sign of the dispersion coefficient. The pre-compensation just contributes a multiplicative phasor term to the kernel and does not change its magnitude; hence it plays no role in the regime where the GN model applies. Note that the kernel $\mathcal{K}$ in Eq. (1) depends only on the product $v \equiv f_1 f_2$. It can be generalized to include third-order dispersion [5, 9].

Now, for any link with or without dispersion management (DM) for which the GN model applies, one just has to calculate the link kernel function $\mathcal{K}$ and then use (1) to get the NLI PSD. For multispan links, the kernel factorizes as

$$\mathcal{K}(v) = \mathcal{K}(0)\chi(v)\eta_1(v) \qquad (3)$$

where $\chi(v)$ is the phased-array term [10], and $\eta_1(v)$ is the single-span normalized kernel. In all numerical examples we will use a terrestrial transmission system with N identical compensated fiber spans with lumped end-span amplification and uncompensation ratio ζ ($\zeta = 1$ for DU links, and $\zeta = 0$ for full in-line compensation), and dispersion β_2, attenuation α and span length z_A. The kernel at $L = Nz_A$ is given by (3), where [11]: $\mathcal{K}(0) = N\gamma\frac{1-\mathrm{e}^{-\alpha z_A}}{\alpha z_A}$,

$$\chi(v) = \frac{1}{N}\sum_{k=1}^{N} \mathrm{e}^{-j(k-1)\beta_2 z_A \zeta (2\pi)^2 v}, \quad \text{and} \quad \eta_1(v) = \frac{1-\mathrm{e}^{-\alpha z_A(1-j\frac{\beta_2}{\alpha}(2\pi)^2 v)}}{(1-\mathrm{e}^{-\alpha z_A})(1-j\frac{\beta_2}{\alpha}(2\pi)^2 v)}.$$

Substitution of Eq. (3) into Eq. (1) yields the explicit NLI PSD in [1, 2]. The system function $|\mathcal{K}((f_1-f)\cdot(f_2-f))/\mathcal{K}(0)|^2$ is the four-wave mixing (FWM) efficiency at frequency f for pumps placed at frequencies f_1, f_2, and f_1+f_2-f [2, 10, 12].

The trouble with the analytic formula (1) is that it involves a double frequency integration where the squared kernel $|\mathcal{K}(f_1 f_2)|^2$ is oscillating in frequency faster and faster as the number of spans increases because of the phased-array term and poses non-trivial integration problems [2]. Integration is eased by a suitable change of integration variables. In [2] the change to

hyperbolic coordinates $u = -\frac{1}{2}\ln(f_2/f_1)$, $v = \sqrt{f_1 f_2}$ was proposed. The rationale was that the squared kernel is a function of v only, hence at fixed v, integration in the (f_1, f_2) plane follows the constant contour levels of $|\mathcal{K}(f_1 f_2)|^2$. With a similar rationale, we use here the equivalent but formally simpler change $u = f_1$, $v = f_1 f_2$, whose Jacobian is $J = u$ and whose inverse is $f_1 = u$, $f_2 = v/u$. With such a change, the double integral $I(f)$ on the (f_1, f_2) plane becomes

$$
I(f) = \int_0^\infty |\mathcal{K}(v)|^2 \left[\int_0^\infty \frac{1}{u} G(f+u) G(f+\frac{v}{u}) G(f+u+\frac{v}{u}) \mathrm{d}u \right.
$$
$$
+ \int_0^\infty \frac{1}{u} G(f-u) G(f+\frac{v}{u}) G(f-u+\frac{v}{u}) \mathrm{d}u + \int_0^\infty \frac{1}{u} G(f-u) G(f-\frac{v}{u}) G(f-u-\frac{v}{u}) \mathrm{d}u
$$
$$
\left. + \int_0^\infty \frac{1}{u} G(f+u) G(f-\frac{v}{u}) G(f+u-\frac{v}{u}) \mathrm{d}u \right] \mathrm{d}v \tag{4}
$$

where the four terms in the square bracket correspond to integration over the four quadrants.

When the input WDM signals have rectangular spectra, the square-bracketed integrals in Eq. (4) can be solved exactly. In the next sections we present single-integral formulas of the NLI PSD in such a case. These formulas allow to quickly determine whether single- or cross-channel nonlinearity dominates, and provide a case against which numerical double-integration routines of Eq. (1) can be checked for accuracy. Starting from these formulas, new simplified expressions are also derived at zero frequency. We present first the Nyquist-WDM case, and then the non-Nyquist case.

3. NLI PSD for single-channel and Nyquist-WDM systems
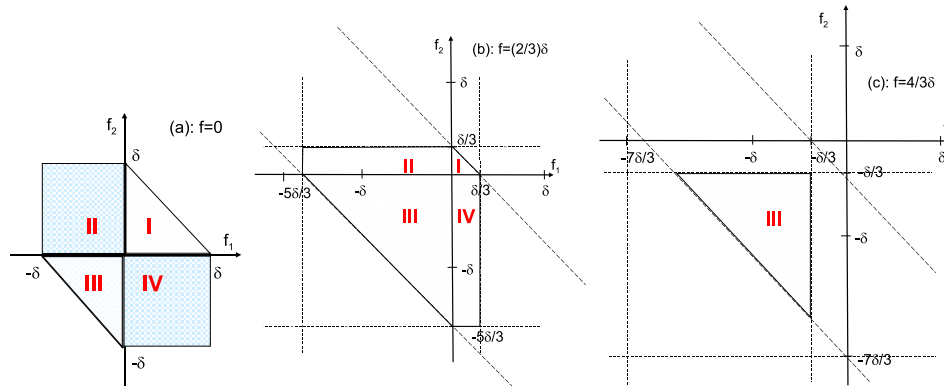
Fig. 1. Domains over which integrand in Eq. (1) is non-zero when input PSD is a gate over $f \in [-\delta, \delta]$. Integration over domains I through IV yields the four lines in Eq. (4).

We tackle here the rectangular-spectrum single-channel case, or equivalently the WDM case where no bandwidth gaps are present between neighboring channels. The total power is P and the input PSD $G(f) = \frac{P}{2\delta}\mathrm{rect}_{2\delta}(f+\delta)$ is a rectangular gate centered at $f = 0$ with total two-sided bandwidth 2δ. The integrand in Eq. (1) is non-zero only over the shaded domains in quadrants I through IV shown in Fig. 1 at several values of f. Note that, since $|\mathcal{K}(v)|^2 = |\mathcal{K}(-v)|^2$ for any kernel, Eq. (2), then the squared kernel is the same over the 4 quadrants, hence the integral in Eq. (1) over quadrants II and IV has always the same value.

We can now state our main result on SCI. Define the normalized double integral $\mathscr{I}(f) \triangleq I(f)/(P/(2\delta))^3$, with $I(f)$ as in Eq. (1). Using Eq. (4), we can prove that $\mathscr{I}(f)$ can be exactly

expressed as follows. If $|f| < \delta$:

$$
\begin{aligned}
\mathscr{I}(f) &= \int_0^{(\frac{\delta-f}{2})^2} |\mathscr{K}(v)|^2 \ln\left(\frac{\frac{\delta-f}{2} + \sqrt{(\frac{\delta-f}{2})^2 - v}}{\frac{\delta-f}{2} - \sqrt{(\frac{\delta-f}{2})^2 - v}} \right) dv + 2\int_0^{\delta^2 - f^2} |\mathscr{K}(v)|^2 \ln\left(\frac{\delta^2 - f^2}{v} \right) dv \\
&+ \int_0^{(\frac{\delta+f}{2})^2} |\mathscr{K}(v)|^2 \ln\left(\frac{\frac{\delta+f}{2} + \sqrt{(\frac{\delta+f}{2})^2 - v}}{\frac{\delta+f}{2} - \sqrt{(\frac{\delta+f}{2})^2 - v}} \right) dv
\end{aligned}
\tag{5}
$$

else if $\delta \le |f| < 3\delta$:

$$
\mathscr{I}(f) = \int_{(|f|-\delta)^2}^{2\delta(|f|-\delta)} |\mathscr{K}(v)|^2 \ln\left(\frac{v}{(|f|-\delta)^2} \right) dv + \int_{2\delta(|f|-\delta)}^{(\frac{\delta+|f|}{2})^2} |\mathscr{K}(v)|^2 \ln\left(\frac{\frac{\delta+|f|}{2} + \sqrt{(\frac{\delta+|f|}{2})^2 - v}}{\frac{\delta+|f|}{2} - \sqrt{(\frac{\delta+|f|}{2})^2 - v}} \right) dv
\tag{6}
$$

otherwise $\mathscr{I}(f) = 0$. Since $\sup(|\mathscr{K}(v)|) < \infty$ and each log term in Eqs. (5) and (6) is integrable, $\mathscr{I}(f)$ is well defined. For $f > 0$, the first integral in Eq. (5) corresponds to integration over domain I in Fig. 1, the second term to integration over domains II+IV, and the last term over domain III. When $\delta \le f < 3\delta$ only domain III is nonzero. Details of proof are found in [13]. For a 20x100km DU link at various values of the transmission fiber dispersion, Fig. 2(a) shows
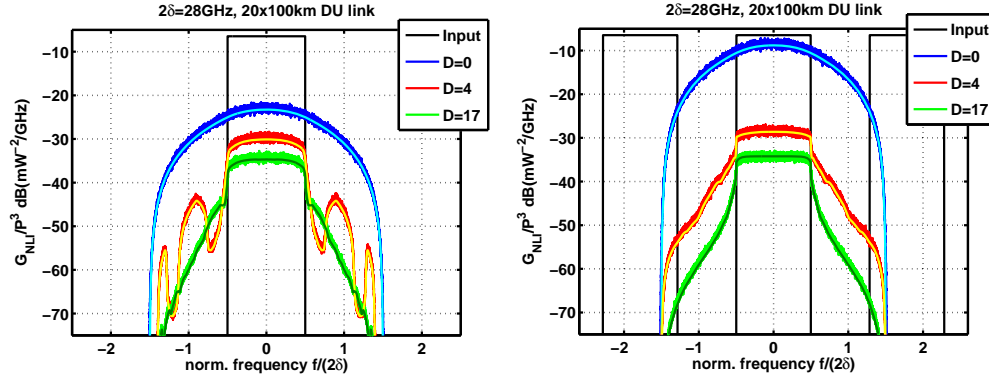
Fig. 2. NLI normalized spectra vs. frequency (normalized to bandwidth $2\delta = 28$GHz) for channels with rectangular input PSD at three dispersion values D (ps/nm/km) for 20x100km DU link. Kernel (3) had $\alpha = 0.2$dB/km, $\zeta = 1$, $\gamma = 1.27(\text{W km})^{-1}$. Theory: cyan, yellow, dark green curves. SSF simulations: blue, red, green curves. (a) $G_{NLI}(f)/P^3$ for single channel, theory Eqs. (5) and (6); (b) $G_{XCI}(f)/P^3$ on central channel for $M = 15$ channels at $\Delta = 50$GHz, theory Eqs.(13) and (14).

the theoretical normalized NLI PSD $\frac{G_{NLI}(f)}{P^3} = \frac{16}{27} \mathscr{I}(f)/(2\delta)^3$ obtained from Eqs. (5) and (6) and numerically solved with the *quadgk* integration routine of Matlab. The kernel is given by Eq. (3). To double-check theory, Monte-Carlo simulated NLI spectra are also shown. They were estimated by the periodogram method [14] over a window of 2^{17} samples, and were obtained by using as input signal to the SSF propagator [15] a -40dBm complex Gaussian noise with a 28GHz rectangular spectrum. The periodogram was averaged over 100 realizations.

The next 3 subsections are introduced to explore the accuracy of the *flat-PSD approximation* used in Poggiolini's approximations of the NLI power [2].

3.1. SCI PSD at zero frequency

From Eq. (5), the value at $f = 0$ is found as:

$$\mathscr{I}(0) = 2\int_0^{(\frac{\delta}{2})^2} |\mathscr{K}(v)|^2 \ln\left(\frac{\frac{\delta}{2} + \sqrt{(\frac{\delta}{2})^2 - v}}{\frac{\delta}{2} - \sqrt{(\frac{\delta}{2})^2 - v}}\right) dv + 2\int_0^{\delta^2} |\mathscr{K}(v)|^2 \ln\left(\frac{\delta^2}{v}\right) dv. \quad (7)$$

Referring to [2, Fig. 1] or Fig. 1(a), the first term in the above sum corresponds to integration of $|\mathscr{K}(f_1 f_2)|^2$ over the triangular domains in the I+III quadrants, while the second term to the square domains in quadrants II+IV. When the squared half-bandwidth δ^2 is much larger than the 3-dB bandwidth of the squared kernel $|\mathscr{K}(v)|^2$, the triangular domains in quadrants I and III can be replaced with squared domains as in quadrants II and IV, thus getting the upper-bound

$$\mathscr{I}(0) \lesssim 4\int_0^{\delta^2} |\mathscr{K}(v)|^2 \ln\left(\frac{\delta^2}{v}\right) dv \quad (8)$$

that together with Eq. (2) specializes to [4, eq. (6)] for a DU link. The corresponding squared integration domain in the (f_1, f_2) plane matches domain $\mathscr{Q}$ in [2, Fig. 24].

3.2. SCI PSD at zero dispersion

When dispersion tends to zero, any kernel becomes frequency-independent: $\mathscr{K}(v) \equiv \mathscr{K}(0)$ at all v. In this case, it may be verified that Eqs. (5) and (6) tend to:

$$\mathscr{I}(f) = \begin{cases} 3\delta^2 - f^2 & \text{if } |f| < \delta \\ (3\delta - |f|)^2/2 & \text{if } \delta \leq |f| < 3\delta \end{cases} \quad (9)$$

and zero otherwise. Such a result can also be double-checked directly from Eq. (1) by simple geometric considerations. Equation (9) was plotted in cyan in Fig. 2(a).

3.3. Accuracy of flat-PSD approximation for SCI and Nyquist WDM

For an M-channel Nyquist-WDM system with per-channel power P and bandwidth 2δ, the NLI PSD is given by $G_{NLI}(f) = \frac{16}{27}I(f)$, with $I(f) = (\frac{PM}{2\delta M})^3 \mathscr{I}(f)$, and $\mathscr{I}(f)$ explicitly given in Eqs. (5) and (6) where we substitute $\delta \rightarrow M\delta$. After receiver matched filtering with $H(f) = 1$ for $|f| < \delta$ and zero else (Appendix A), the total NLI power on the reference central channel can be conveniently written by introducing the average value $\overline{\mathscr{I}} \triangleq \frac{1}{2\delta}\int_{-\delta}^{\delta} \mathscr{I}(f) df$ as:

$$P_{NLI} = \frac{16}{27}\left(\frac{P}{2\delta}\right)^3 \int_{-\delta}^{\delta} \mathscr{I}(f) df \equiv \frac{16}{27}P^3 \frac{\overline{\mathscr{I}}}{(2\delta)^2}. \quad (10)$$

For WDM computations, it is common practice to adopt the flat-PSD approximation, i.e., assume instead that $\mathscr{I}(f)$ is flat at its $\mathscr{I}(0)$ value over the receiver bandwidth 2δ, so that $\overline{\mathscr{I}}$ is replaced by $\mathscr{I}(0)$ in Eq. (10) [1–3]. Such an assumption leads to an over-estimation of the NLI power by an amount $\mathscr{O} \triangleq \mathscr{I}(0)/\overline{\mathscr{I}}$. For instance, at zero dispersion and assuming a Nyquist-WDM system with M channels, we get from Eq. (9): $\overline{\mathscr{I}} = \frac{1}{\delta}\int_0^{\delta}(3(M\delta)^2 - f^2) df = \delta^2(3M^2 - \frac{1}{3})$, and $\mathscr{I}(0) = 3(M\delta)^2$, hence

$$\mathscr{O} = 1/(1 - \frac{1}{9M^2}) \quad (11)$$

and this result is valid at any WDM bandwidth when dispersion is zero, or equivalently when bandwidth tends to zero at any nonzero dispersion. The worst over-estimation occurs when
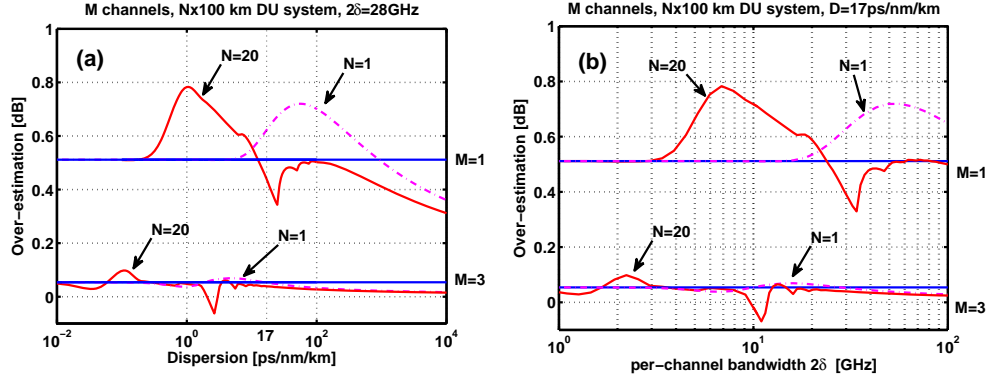
Fig. 3. Over-estimation $\mathcal{O}$ in an M-channel Nyquist-WDM Nx100km DU system with each channel having rectangular spectrum of bandwidth 2δ. **(a)** versus fiber dispersion D at $2\delta = 28$GHz; **(b)** versus 2δ, at $D = 17$ps/nm/km. Blue lines: value at $D = 0$, Eq. (11).

$M = 1$ and equals $\mathcal{O} = 9/8$, i.e., 0.51 dB. For $M > 1$ the dB value may be well approximated as $\mathcal{O}^{dB} \cong \frac{0.5}{M^2}$ and very quickly vanishes as M increases.

Figure 3 shows the over-estimation $\mathcal{O}$ for an M-channel Nyquist-WDM signaling over an Nx100 km DU link when the per-channel spectra are rectangular of bandwidth 2δ, plotted versus (a) fiber dispersion D at $2\delta = 28$ GHz, and (b) versus 2δ at $D = 17$ps/nm/km. The top group of curves refer to single-channel ($M = 1$), the bottom group of curves to an $M = 3$ system. In Fig. 3(a) we see that at small D the over-estimation converges to the analytical value (11) (reported as a solid blue horizontal line), and as $D \to \infty$ the over-estimation fades to 0 dB. For $M = 1$ we get the largest over-estimation $\mathcal{O}_{max}^{dB} \sim 0.78$. When we increase the Nyquist-WDM channels to $M \geq 3$ the over-estimation fluctuates around the zero-dispersion value Eq. (11) by less than 0.054 dB. The negative $\mathcal{O}^{dB} = -0.06$ value at $N = 20$, $D = 2.65$ ps/nm/km is due to a dip at $f = 0$ of the NLI PSD such that the maximum of the PSD is away from $f = 0$. The curves in Fig. 3(b) provide a horizontal-axis rescaling of those in Fig. 3(a) because the NLI PSD Eq. (1) scales with the parameter $D\delta^2$. This is due to the fact that the kernel $\mathcal{K}(v)$ in Eq. (2) is a function of the parameter $\beta_2 v$, which is proportional to $Df_1 f_2$. The take-away message from Fig. 3 is that for practical values of $M \geq 3$ in Nyquist-WDM DU systems at any dispersion and per-channel bandwidth we can safely use $\mathcal{I}(0)$ in place of the more demanding $\overline{\mathcal{I}}$ when evaluating the NLI power in Eq. (10).

4. NLI PSD for Non-Nyquist WDM systems

We assume here a WDM system with a reference central channel, N_c channels to its left and N_c channels to its right on the frequency axis, hence $M = 2N_c + 1$ channels, with uniform frequency spacing Δ. The WDM comb has input PSD $G(f) = \sum_{k=-N_c}^{N_c} S(f - k\Delta)$, where *each* lowpass equivalent channel envelope has power P and a rectangular PSD with bandwidth 2δ, namely $S(f) = \frac{P}{2\delta}\mathrm{rect}_{2\delta}(f + \delta)$. Channels do not spectrally overlap, hence $2\delta < \Delta$. The domain of integration in the double-integral in Eq. (1) is the set of *islands* depicted at $f = 0$ in Fig. 4 (Cfr. [2, Fig. 3]). Integration over the central red island yields the SCI and can directly be obtained from Eqs. (5) and (6). Integration over the on-axes yellow islands yields the XCI, and integration over all off-axes islands yields the multi-channel interference (MCI) [2]. Hence the NLI PSD may be decomposed as the sum of SCI, XCI, and MCI contributions: $G_{NLI}(f) = G_{SCI}(f) + G_{XCI}(f) + G_{MCI}(f)$. Highly dispersed systems quite effectively suppress MCI (i.e., the classical FWM), so that XCI is the relevant cross-nonlinearity, and encompasses both scalar
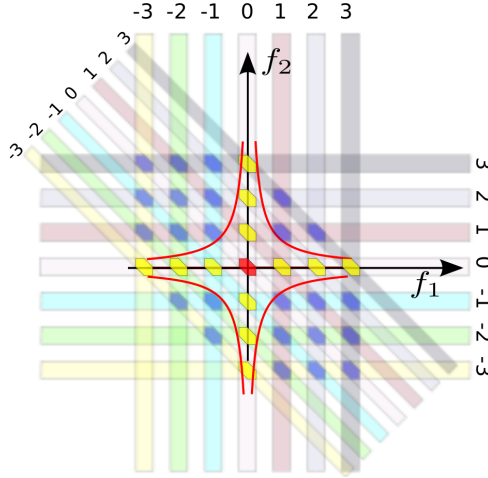
Fig. 4. Integration domain in Eq. (1) given at $f = 0$ by intersection of support of $G(f + f_2)$ (horizontal stripes), $G(f + f_1)$ (vertical) and $G(f + f_1 + f_2)$ (tilted). Red island = SCI. Yellow islands = XCI. Blue islands = MCI. Red curves: contours of $|\mathscr{K}(f_1 f_2)|^2$.

cross-phase modulation and cross-polarization modulation [16]. The XCI PSD is obtained from Eq. (1) as $G_{XCI}(f) = \frac{16}{27} I_{XCI}(f)$, with $I_{XCI}(f) \triangleq 2 \sum_{m=1}^{N_c} (I_m(f) + I_{-m}(f))$ (the term 2 is the degeneracy factor), and we defined

$$I_m(f) \triangleq \iint\limits_{-\infty}^{\infty} |\mathscr{K}(f_1 f_2)|^2 G_0(f + f_1) G_m(f + f_2) G_m(f + f_1 + f_2) \mathrm{d}f_1 \mathrm{d}f_2 \qquad (12)$$

with $G_m(f) = S(f - m\Delta)$ the m-th channel PSD. We can now state our main result on XCI.

We can prove that for any integer $m > 0$ the normalized double integral $\mathscr{I}_m(f) \triangleq (I_m(f) + I_{-m}(f))/(P/2\delta)^3$ can be written as follows. Define $(\eta, \eta_m^+, \eta_m^-) \triangleq (\delta - |f|, m\Delta + \eta, m\Delta - \eta)$ and $(\varepsilon, \varepsilon_m^+, \varepsilon_m^-) \triangleq (\delta + |f|, m\Delta + \varepsilon, m\Delta - \varepsilon)$. Then, if $|f| < \delta$:

$$
\begin{aligned}
\mathscr{I}_m(f) = {} & \int_0^{\eta \varepsilon_m^-} |\mathscr{K}(v)|^2 \ln \left(\frac{\frac{v}{\varepsilon_m^-}}{\frac{\eta_m^+}{2} - \sqrt{(\frac{\eta_m^+}{2})^2 - v}} \right) \mathrm{d}v + \int_{\eta \varepsilon_m^-}^{\eta m \Delta} |\mathscr{K}(v)|^2 \ln \left(\frac{\eta}{\frac{\eta_m^+}{2} - \sqrt{(\frac{\eta_m^+}{2})^2 - v}} \right) \mathrm{d}v \\[4pt]
& + \int_0^{\eta m \Delta} |\mathscr{K}(v)|^2 \ln \left(\frac{-\frac{\eta_m^-}{2} + \sqrt{(\frac{\eta_m^-}{2})^2 + v}}{\frac{v}{\varepsilon_m^+}} \right) \mathrm{d}v + \int_{\eta m \Delta}^{\eta \varepsilon_m^+} |\mathscr{K}(v)|^2 \ln \left(\frac{\eta \varepsilon_m^+}{v} \right) \mathrm{d}v \\[4pt]
& + \int_0^{\varepsilon m \Delta} |\mathscr{K}(v)|^2 \ln \left(\frac{-\frac{\varepsilon_m^-}{2} + \sqrt{(\frac{\varepsilon_m^-}{2})^2 + v}}{\frac{v}{\eta_m^+}} \right) \mathrm{d}v + \int_{\varepsilon m \Delta}^{\varepsilon \eta_m^+} |\mathscr{K}(v)|^2 \ln \left(\frac{\varepsilon \eta_m^+}{v} \right) \mathrm{d}v \\[4pt]
& + \int_0^{\varepsilon \eta_m^-} |\mathscr{K}(v)|^2 \ln \left(\frac{\frac{v}{\eta_m^-}}{\frac{\varepsilon_m^+}{2} - \sqrt{(\frac{\varepsilon_m^+}{2})^2 - v}} \right) \mathrm{d}v + \int_{\varepsilon \eta_m^-}^{\varepsilon m \Delta} |\mathscr{K}(v)|^2 \ln \left(\frac{\varepsilon}{\frac{\varepsilon_m^+}{2} - \sqrt{(\frac{\varepsilon_m^+}{2})^2 - v}} \right) \mathrm{d}v
\end{aligned}
\tag{13}
$$

else if $\delta \le |f| < 3\delta$:

$$
\begin{aligned}
\mathscr{I}_m(f) = {} & \int_{-\eta(\varepsilon_m^- - \eta)}^{-\eta \eta_m^+} |\mathscr{K}(v)|^2 \ln \left(\frac{\frac{\varepsilon_m^-}{2} - \sqrt{(\frac{\varepsilon_m^-}{2})^2 + v}}{\eta} \right) \mathrm{d}v + \int_{-\eta \eta_m^+}^{2\delta \eta_m^+} |\mathscr{K}(v)|^2 \ln \left(\frac{-\frac{\varepsilon_m^-}{2} + \sqrt{(\frac{\varepsilon_m^-}{2})^2 + v}}{\frac{v}{\eta_m^+}} \right) \mathrm{d}v \\[4pt]
& + \int_{-\eta \eta_m^-}^{-\eta(\varepsilon_m^+ + \eta)} |\mathscr{K}(v)|^2 \ln \left(\frac{v}{-\eta \eta_m^-} \right) \mathrm{d}v + \int_{-\eta(\varepsilon_m^+ + \eta)}^{2\delta \eta_m^-} |\mathscr{K}(v)|^2 \ln \left(\frac{\frac{v}{\eta_m^-}}{\frac{\varepsilon_m^+}{2} - \sqrt{(\frac{\varepsilon_m^+}{2})^2 - v}} \right) \mathrm{d}v
\end{aligned}
\tag{14}
$$

otherwise $\mathscr{I}_m(f) = 0$. Since $\sup(|\mathscr{K}(v)|) < \infty$ and each log term in Eqs. (13) and (14) is integrable, $\mathscr{I}_m(f)$ is well defined. The details of the proof can be found in [13]. For a 15-channel WDM system with rectangular signal spectra over a 20x100km DU link, Fig. 2(b) shows $\frac{G_{XCI}(f)}{P^3} = \frac{16}{27} I_{XCI}(f)$ obtained from Eqs. (13) and (14), at various values of the transmission fiber dispersion D (ps/nm/km). SSF simulated XCI spectra are also shown to double-check theory. They were obtained by separate-field SSF propagation (which does not account for MCI [15]) of 15 input Gaussian processes with -40dBm power and 28GHz rectangular spectra spaced by $\Delta = 50$GHz, with the self-phase modulation operator deactivated on the central channel. Figure 2(b) shows that the XCI PSD at typical dispersions is flatter over the signal bandwidth than the corresponding SCI PSD in Fig. 2(a).

4.1. XCI PSD at zero frequency and new upper-bound

As a corollary, the value at $f = 0$ is found from Eq. (13) as follows. Define $\Delta_m^+ \triangleq m\Delta + \delta$ and $\Delta_m^- \triangleq m\Delta - \delta$. Then,

$$
\mathscr{I}_m(0) = 2\{ \int_0^{\delta\Delta_m^-} |\mathscr{K}(v)|^2 \ln\left(\frac{\frac{v}{\Delta_m^-}}{\frac{\Delta_m^+}{2} - \sqrt{(\frac{\Delta_m^+}{2})^2 - v}} \right) dv + \int_{\delta\Delta_m^+}^{\delta m\Delta} |\mathscr{K}(v)|^2 \ln\left(\frac{\delta}{\frac{\Delta_m^+}{2} - \sqrt{(\frac{\Delta_m^+}{2})^2 - v}} \right) dv
$$
$$
+ \int_0^{\delta m\Delta} |\mathscr{K}(v)|^2 \ln\left(\frac{-\frac{\Delta_m^-}{2} + \sqrt{(\frac{\Delta_m^-}{2})^2 + v}}{\frac{v}{\Delta_m^+}} \right) dv + \int_{\delta m\Delta}^{\delta\Delta_m^+} |\mathscr{K}(v)|^2 \ln\left(\frac{\delta\Delta_m^+}{v} \right) dv \}.
$$

(15)
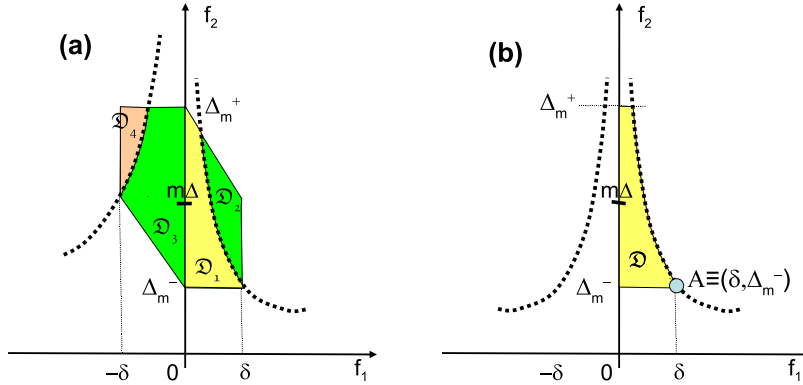
Fig. 5. (a) The four integration domains in the (f_1, f_2)-plane whose integration yields the four v-integral terms in Eq. (15) in the order they appear (see also [13, Fig. 10]). Dashed curves are hyperbolas. (b) Domain $\mathscr{D}$ delimited by hyperbola $v = f_1 f_2 = \delta\Delta_m^-$ passing at point A, approximating squared kernel integral over domain $\mathscr{D}_1$, and also $\mathscr{D}_3$.

Figure 5(a) shows a geometric interpretation of the 4 terms in the curly bracket in (15) as the integral of $|\mathscr{K}(f_1 f_2)|^2$ over the shown domains $\mathscr{D}_1$ through $\mathscr{D}_4$ in the (f_1, f_2) plane, in the order they appear in Eq. (15). Of these, the dominant integrals are over $\mathscr{D}_1$ and $\mathscr{D}_3$, which can both be approximated as the integral over domain $\mathscr{D}$ in Fig. 5(b), and thus

$$
\mathscr{I}_m(0) \cong 4 \iint_{\mathscr{D}} |\mathscr{K}(f_1 f_2)|^2 df_1 df_2 = 4 \int_{v=0}^{\delta\Delta_m^-} \int_{u=v/\Delta_m^+}^{v/\Delta_m^-} |\mathscr{K}(v)|^2 \frac{1}{u} du dv = 4\ln\left(\frac{\Delta_m^+}{\Delta_m^-}\right) \int_0^{\delta\Delta_m^-} |\mathscr{K}(v)|^2 dv
$$

(16)

with the usual change of variables $u = f_1$, $v = f_1 f_2$ as in Eq. (4). Therefore, whenever the product $\delta\Delta$ is far larger than the 3dB bandwidth of the squared kernel $|\mathscr{K}(v)|^2$, we may substitute

$\delta \Delta_m^- \to \infty$ in the top integration limit, so that an upper bound to Eq. (16) is

$$\mathscr{I}_m(0) \lesssim 4 \ln\left(\frac{1 + \frac{\eta/2}{m}}{1 - \frac{\eta/2}{m}}\right) \int_0^\infty |\mathscr{K}(v)|^2 dv \tag{17}$$

where we introduced the bandwidth efficiency $\eta \triangleq \frac{2\delta}{\Delta}$.

4.2. *Zero dispersion XCI PSD and flat-PSD approximation*

At $D = 0$, integration over every XCI island (Cfr Fig. 4) produces the same result, hence the XCI PSD is just $4N_c$ times the SCI PSD in Eq. (9). Thus the estimation error of XCI power at $D = 0$ is again given by expression (11). If we define $\mathscr{I}_{XCI}(f) \triangleq I_{XCI}(f)/(P/2\delta)^3$, similar conclusions regarding the use of $\mathscr{I}_{XCI}(0)$ instead of $\overline{\mathscr{I}}_{XCI}$ in the flat-PSD approximation (Cfr. Eq. (10)) apply.

5. Single- and cross-channel NLI scaling properties

As briefly recalled in Appendix A, the NLI power obtained from the GNRF Eq. (1) enters in the calculation of the signal to noise ratio (SNR) for detection of digitally-modulated signals. Only input signal spectra matter in the GNRF, and not the modulation format [7, 8].

The NLI power can be expressed as $P_{NLI} \triangleq a_{NL}P^3$. We show next how the NLI coefficient a_{NL} scales with the main system parameters, since a_{NL} determines the scaling of both Q-factor [17] and nonlinear threshold [18]. In all the following figures, all analytical curves use the flat-PSD approximation (Sec. 3.3). Since SCI, XCI and MCI PSDs add up, the nonlinear coefficient is the sum of SCI, XCI and MCI contributions: $a_{NL} = a_{SCI} + a_{XCI} + a_{MCI}$. It is reported in all subsequent figures with the label "WDM". For single-channel NLI we use

$$a_{SCI} = \frac{16}{27} \frac{R}{(2\delta)^3} \mathscr{I}(0) \tag{18}$$

where $\mathscr{I}(0)$ is given by Eq. (7) for the SCI (green solid line in all figures), and by Eq. (8) for the SCI UB (green dashed line). As explained in Appendix A, for matched-filter detection of digital signals with rectangular spectra, R plays the role of the signal symbol-rate, and may differ from the matched-filter bandwidth 2δ. The flat-PSD approximation for XCI yields

$$a_{XCI} = \frac{16}{27} \frac{R}{(2\delta)^3} 2 \sum_{m=1}^{N_c} \mathscr{I}_m(0) \tag{19}$$

and uses $\mathscr{I}_m(0)$ in Eq. (15) (in all figures in red solid line). Using instead the UB in Eq. (17) we get our new XCI UB (red dashed line) as

TYPO ~~ln[~~

$$a_{XCI-UB} = \frac{16}{27} \frac{R}{\delta^3} \left[\frac{\Gamma(N_c + 1 + \frac{\eta}{2})\Gamma(1 - \frac{\eta}{2})}{\Gamma(N_c + 1 - \frac{\eta}{2})\Gamma(1 + \frac{\eta}{2})}\right] \int_0^\infty |\mathscr{K}(v)|^2 dv \tag{20}$$

where $\Gamma(z)$ is the Gamma function. The ratio in square brackets is the closed-form of the sum $\sum_{m=1}^{N_c} \ln\left(\frac{1 + \frac{\eta/2}{m}}{1 - \frac{\eta/2}{m}}\right)$, which simplifies to $\ln(2N_c + 1)$ when $\eta = 1$. A good approximation to the above sum at small η is $\eta \sum_{m=1}^{N_c} \frac{1}{m}$, with a worst-case error of 9% at $(N_c, \eta) = (1, 1)$. Using such an approximation in place of the square-bracketed expression in Eq. (20) reveals both the XCI scaling with $1/(2\delta)^2$ at fixed Δ, and the scaling with $\log(N_c)$ at large N_c when η is small [19, 20]. The XCI UB Eq. (20) depends on span number N through the squared-kernel integral. Appendix B provides a general formula linking this integral to the power-weighted

dispersion distribution [21], proves that the squared-kernel integral exactly scales linearly with N for all DU links, and gives its exact expression for lumped end-span amplification and finite span length.

5.1. Scaling with symbol-rate
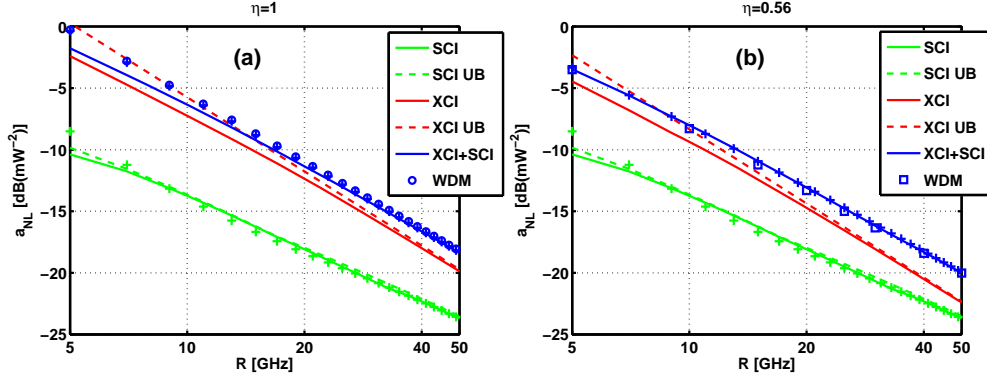
Fig. 6. NLI coefficient [dB(mW^{-2})] versus channel bandwidth $2\delta \equiv R$ [GHz] for SMF DU link with $N = 20$ spans, span length $z_A = 100$km, $M = 81$ channels, at a bandwidth efficiency $\eta = \frac{2\delta}{\Delta} = 1$ (**a**); and $\eta = 0.56$ (**b**). Crosses: [2, eq. (13),(22)].

Figure 6 shows the NLI coefficient versus channel bandwidth $2\delta \equiv R$ for a 20x100 km DU link over standard single-mode fiber (SMF) with $D = 17$ ps/nm/km, for an $M = 81$ channel WDM system at a bandwidth efficiency $\eta = \frac{2\delta}{\Delta} = 1$ (Nyquist-WDM, Fig. 6(a)) and $\eta = 0.56$ (e.g., $\Delta = 50$GHz at $R = 28$Gbaud, Fig. 6(b)). Fixing η implies increasing the channel spacing Δ as R is increased [16]. We see that the NLI coefficient is always decreasing with R, and a decrease as $1/R^2$ is forecast by the XCI UB (20). Besides the SCI, the SCI UB, the XCI and the XCI UB (whose color code was already introduced), we also report in blue solid line the approximation $a_{NL} \cong a_{SCI} + a_{XCI}$ (label XCI+SCI). In the Nyquist-WDM case, Fig. 6(a), the WDM a_{NL} coefficient is analytical (circles) and is obtained from Eq. (18) using for $\mathscr{I}(0)$ Eq. (7) where δ is replaced by $M\delta$. In the non-Nyquist case we do not have an exact analytical WDM formula. Thus in Fig. 6(b) at $\eta = 0.56$ the WDM a_{NL} curve (squares) was obtained through a fast-Fourier-transform (FFT) based direct numerical evaluation of the double frequency integral (1) that yields the whole NLI PSD [9]. The XCI+SCI curve lays slightly above the WDM squares at larger R because of the flat-PSD over-estimation in Eqs. (18) and (19), and increases to match the WDM square at $R = 5$Gbaud because MCI starts to be important at smaller R. Blue and green crosses report the closed-form 'asinh' expressions for WDM and single-channel [2, eq. (13),(22)], obtained by using an effective bandwidth $B_{WDM} = 2\delta M^{2\delta/\Delta}$, and we note the excellent match with the XCI+SCI curve. In the Nyquist-WDM case, Fig. 6(a), the effect of MCI is more clearly visible because of the noticeable difference of the theoretical WDM (circles) and XCI+SCI curves at symbol-rates below 10Gbaud. Crosses again report the closed-form 'asinh' expressions [2, eq. (13),(22)] with an almost perfect match with the exact WDM circles. From Fig. 6 we learn that in this large WDM system on a 20x100km SMF DU link the XCI always dominates the SCI. We also note that the SCI UB over the shown range is always within 0.5dB from the true SCI value (the 'asinh' approximation is here poor below 20GHz [2]), while the XCI bound for Nyquist-WDM is within 0.5dB of the true XCI value at symbol-rates above 23Gbaud, and above 16Gbaud for the non-Nyquist $\eta = 0.56$ system.

5.2. Scaling with bandwidth efficiency
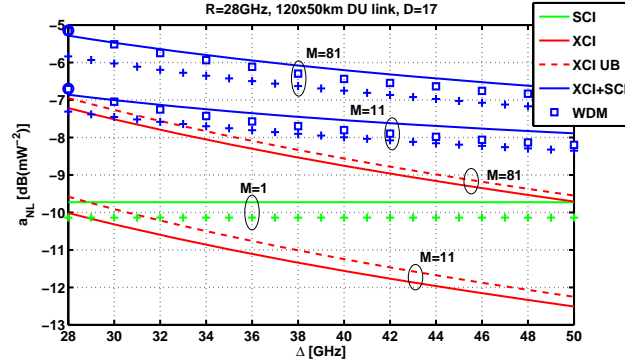
Fig. 7. NLI coefficient [dB(mW^{-2})] vs. channel spacing Δ [GHz], at fixed channel bandwidth $2\delta \equiv R$, for 120×50km SMF DU link, and $M = [1, 11, 81]$ channels. Crosses: [2, eq. (13),(22)].

Figure 7 illustrates the use of the analytical formulas to quickly determine the dominant nonlinear effect in a very long 120x50km SMF DU link with either 11 or 81 WDM channels, as the symbol-rate is fixed to 28 Gbaud and the channel spacing ranges from 28GHz (Nyquist-WDM case) up to 50GHz. While the SCI is independent of Δ, the XCI clearly decreases as the spacing Δ is increased. We see that at $\Delta = 50$GHz ($\eta = 0.56$) and 11 channels the SCI is the dominant effect (Cfr [16, Fig.1], where the number of channels was $M = 11$ at $R \geq 15$Gbaud), but as the channel count is increased to 81 the SCI and XCI give equal nonlinear contributions. For the Nyquist-WDM case $\Delta = 28$GHz, XCI is the dominant effect at both channel counts. Again, note the tightness of the XCI UB, which improves at increasing channel count. We also reported both the XCI+SCI (blue curve) and the WDM (blue squares) obtained by the FFT-based numerical integrator [9] that calculates the whole NLI PSD. The XCI+SCI curve is within 0.3dB of the WDM 'true value' (blue squares) because of the flat-PSD approximation in Eqs. (18) and (19) and not because of the presence of MCI, as we could verify by removing the flat-PSD approximation and using the complete analytical NLI PSD calculated through Eqs. (5) and (6) and Eqs. (13) and (14). We verified that the flat-PSD approximation only gives an over-estimation of the SCI curve (shown as the $M = 1$ curve in Fig. 3), while the XCI curve has essentially no over-estimation. As predicted in Section 3.3, the over-estimation disappears in the Nyquist-WDM case, as confirmed by the coincidence of the WDM square with the analytical WDM value that uses Eq. (18) (blue circles at $\Delta = 28$GHz in Fig. 7). Blue and green crosses also report the closed-form 'asinh' expressions [2, eq. (13),(22)].

5.3. A flat input spectrum is optimal

Figure 8 illustrates the use of the new analytical formulas to quickly verify that the best supporting pulse in a digital optical transmission is the one that achieves the broadest input spectrum [22] (Cfr discussion at end of Appendix A). Figure 8(a) shows the input spectrum for a WDM transmission with fixed per-channel power, with channel spacing $\Delta = 50$GHz, per-channel symbol-rate $R = 5$Gbaud, and a variable pulse bandwidth (i.e., per-channel PSD bandwidth), ranging from the symbol-rate ($2\delta = R$, green PSD), up to the no-spectral overlap limit ($2\delta = \Delta$, red PSD). Figure 8(b) shows the NLI coefficient versus channel bandwidth 2δ over the range delimited by the two extreme cases (green, red) depicted in Fig. 8(a). We observe that both SCI and XCI monotonically decrease as the channel bandwidth increases up to its top
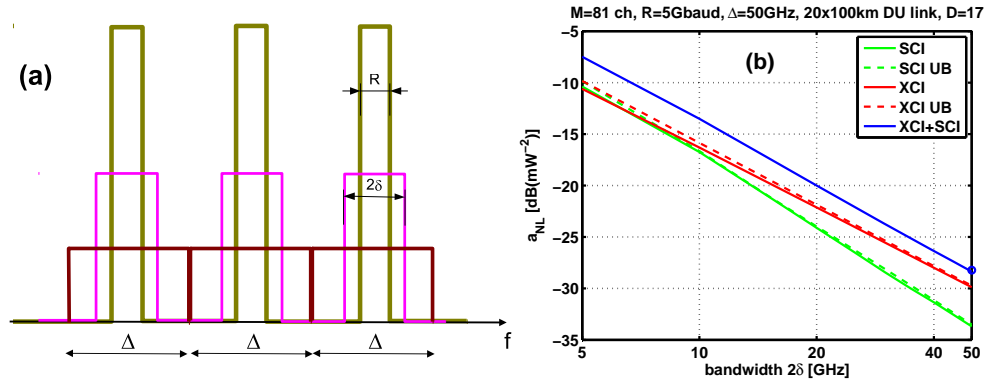
Fig. 8. **(a)** Input WDM spectra at increasing per-channel bandwidth 2δ. **(b)** NLI coefficient vs. channel bandwidth 2δ, at fixed symbol-rate $R = 5$Gbaud, for SMF $20x100$km DU link, $M = 81$ channels, $\Delta = 50$GHz spacing. Blue circle at Nyquist-WDM case $2\delta = 50$GHz gives the analytical WDM value.

limit Δ. Hence we conclude that in order to minimize nonlinearity and thus maximize signal-to-noise ratio one needs to choose $2\delta = \Delta$, i.e., a flat input WDM spectrum (red spectrum in Fig. 8(a)). As the channel bandwidth is increased, we also note that XCI decreases more slowly than SCI, since clearly the gap between channels is decreasing to zero thus favoring XCI. However, notwithstanding closer channel spectra, the frequency enlargement of per-channel input PSD brings about a global decrease also for XCI; from Eq. (20) it is clear that at fixed spacing Δ and symbol-rate R, the XCI power decreases almost as $a_{XCI-UB} \propto 1/(2\delta)^2$. For all realistic kernels we find a minimum when a flat input WDM spectrum is achieved. Although our numerical study is based on rectangular spectra, a simple theoretical explanation of the optimality of a flat input spectrum is proposed in [9]. As a last observation, please note the excellent accuracy of both the SCI and XCI upper-bounds in this numerical experiment.

5.4. Scaling with number of spans

Finally, Fig. 9 illustrates the use of the analytical formulas to explain the different accumulation rates of SCI and XCI as the number of spans N increases [18, 20]. As in [18], we consider transmission of a 19-channel WDM system with per-channel bandwidth/symbol-rate $2\delta = R = 28$Gbaud over an $N \times 50$km SMF DU link. The top row of figures refers to the Nyquist-WDM case ($\eta = 1$) with channel spacing $\Delta = 28$GHz, and the bottom row to the case $\Delta = 50$GHz ($\eta = 0.56$). The left-column figures show the NLI coefficient a_{NL}[dB(mW^{-2})] versus N (in log scale), while blue and green crosses report the closed-form 'asinh' expressions for WDM and single-channel, respectively [2, eq. (13),(22)]. The right-column figures show the local slope $(1 + \varepsilon)$ [dB/dB] of the left-column a_{NL} curves [2, 18]. An explicit formula of the SCI slope parameter ε can be derived from the a_{NL} formula for DU links in [11] as

$$\varepsilon = \frac{1}{\ln(N) + \frac{1}{2}\ln(\frac{4\mu}{\sqrt{5}}(\alpha z_A)^2 \frac{|\beta_2|}{\alpha}R^2)} \tag{21}$$

with a (baud-rate dependent [11]) fitting factor $\mu = 13$. In Figs. 9(b)–9(d) the formula is plotted in dashed line, while crosses report the ε formula in [2, eq. (22)]. We observe from the figure that SCI has a larger slope (i.e., accumulation rate) than XCI, and that the overall slope (that of the XCI+SCI curve, which in the Nyquist-WDM case is also verified to be practically coincident with the exact WDM case) is a weighted average of SCI and XCI slopes [20]. The
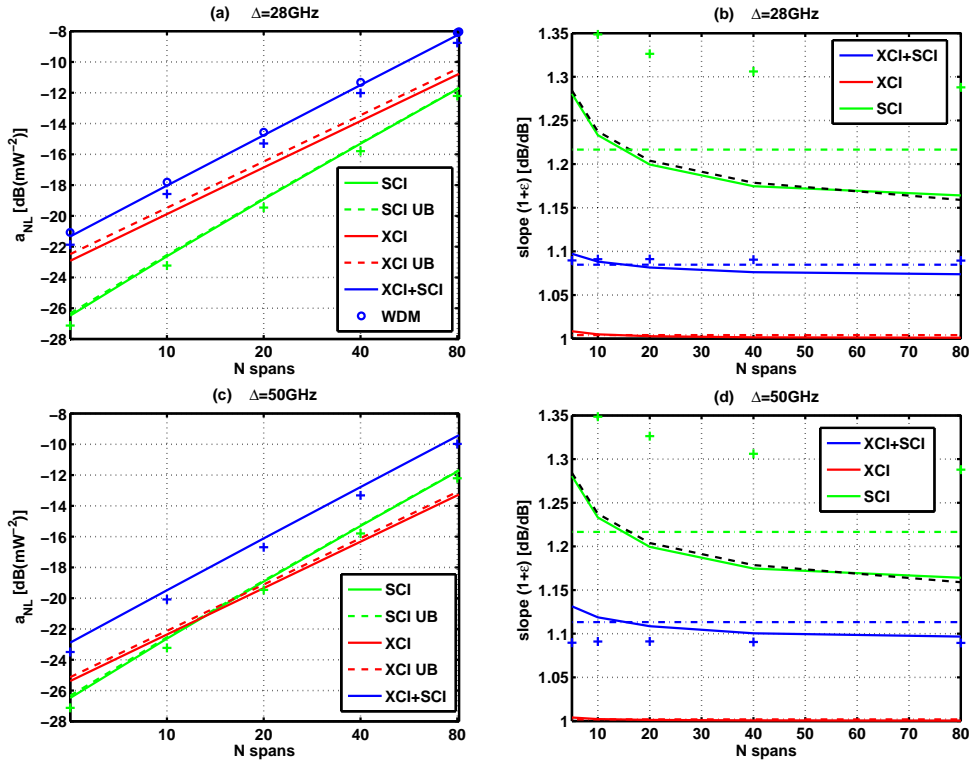
Fig. 9. **(a),(c)**: NLI coefficient versus spans N (log scale) at fixed bandwidth/symbol-rate $2\delta = R = 28$Gbaud, for SMF DU link with span length $z_A = 50$km, and $M = 19$ channels. **(b),(d)**: local slope [dB/dB] of log-log plots in (a),(c) versus N. Dash-dotted: average slope. Black dashed: ε-fit Eq. (21). Crosses: [2, eq. (13),(22)].

XCI slope for the DU link is always close to 1. The reason is the uncorrelation of the spans NLI contributions [2, 11] and is well explained by the XCI UB (20) and the already-mentioned linear scaling with N of the squared-kernel integral for DU links.

6. Conclusions

We provided new semi-analytic formulas of the PSD of the received nonlinear interference in coherent optical links for which the GN model applies. These formulas can be used to both discriminate single- and cross-channel nonlinearity, and to check the accuracy of numerical routines that solve the GNRF double frequency integral (1). Such numerical routines are useful for instance in mixed-fiber links where simple 'asinh' formulas [2] do not exist. A novel bound for XCI was obtained that clearly reveals the major XCI scaling laws, and can find use in path routing in future elastic optical networks. We tested in numerical case studies the accuracy of both the bound and the 'asinh' formulas [2] against the new exact analytical formulas.

Appendix A

Assume that the generic digitally modulated optical signal field (in units of $\sqrt{W}$) is $s(t) = \sum_n I_n g(t - nT)$, with i) I_n the zero-mean dimensionless complex modulating symbol at slot n, with $E[|I_n|^2] = 1$; symbols at different slots are independent; ii) $T = 1/R$ [sec] the symbol time and R the symbol rate; iii) $g(t)$ [$\sqrt{W}$] the supporting pulse with Fourier transform $\tilde{g}(f)$.

The PSD of the cyclostationary signal $s(t)$ is $G(f) = R|\tilde{g}(f)|^2$ $[\frac{W}{Hz}]$ [23]. Signal power is P. Hence $\int_{-\infty}^{\infty} |\tilde{g}(f)|^2 df = \frac{P}{R}$. If at the receiver we use a matched filter with response $H(f) = \tilde{g}^*(f)$, then $\int_{-\infty}^{\infty} |H(f)|^2 df = \frac{P}{R}$, and the matched filtering of pulse $g(t)$ at the best sampling time $t = 0$ gives the pulse energy $\mathscr{E} = P/R$. If $\frac{N_0}{2}$ is the amplified noise white PSD, and the NLI is also white with PSD $G_{NLI}(0)$, then the SNR at matched filter sampled output is

$$SNR = \frac{\mathscr{E}^2}{(\frac{N_0}{2} + G_{NLI}(0))\frac{P}{R}} = \frac{P}{(\frac{N_0}{2} + G_{NLI}(0))R} \tag{22}$$

i.e., the NLI power in the SNR formula [17, 24] is $P_{NLI} = G_{NLI}(0)R$ for every supporting pulse shape, provided that matched filtering is used. Playing with the pulse shape $g(t)$, or equivalently with the per-channel spectrum $G(f)$, however, changes the NLI PSD $G_{NLI}(0)$ given by (1). Thus the NLI power, at a given per-channel power P and symbol rate R, can be minimized by the most appropriate pulse choice, thus maximizing SNR and performance [22].

Appendix B

In this Appendix we wish to provide the exact value of the integral $\int_0^\infty |\mathscr{K}(v)|^2 dv$ for a DU terrestrial link with N identical spans of length z_A, and transmission fibers with nonlinear coefficient γ, attenuation α and dispersion β_2. Let's define $w \triangleq 2\pi v$, and the normalized kernel as $\tilde{\eta}(w) \triangleq \frac{\mathscr{K}(\frac{w}{2\pi})}{\mathscr{K}(0)}$, where $\mathscr{K}(0)$ is a real quantity related to the nonlinear phase as $\Phi_{NL} = P\mathscr{K}(0)$ (see [11], Appendix 4). The power-weighted dispersion distribution (PWDD) $J(c)$ is the (real) "time-domain" Fourier transform of the "frequency-domain" Hermitian function $\tilde{\eta}(w)$ [11,21]. Hence from Parseval: $\int_{-\infty}^{\infty} |\tilde{\eta}(w)|^2 dw = \int_{-\infty}^{\infty} J^2(c) dc$. Also $|\mathscr{K}(v)|^2$ is even in v. Hence

$$I_\infty \triangleq \int_0^\infty |\mathscr{K}(v)|^2 dv = \frac{1}{2} \int_0^\infty |\mathscr{K}(\frac{w}{2\pi})|^2 \frac{dw}{2\pi} = \frac{\mathscr{K}(0)^2}{2} \int_{-\infty}^{\infty} J^2(c) \frac{dc}{2\pi}. \tag{23}$$

This is a general formula that allows the calculation of I_∞ starting from the link PWDD.

Now, consider a DU link with identical spans of length z_A and dispersion β_2. let $\mathscr{K}_1(0)$ and $J_1(c)$ the kernel and PWDD of the single span, respectively. Then $\mathscr{K}(0) = N\mathscr{K}_1(0)$, and ([11, eq. (33)]): $J(c) = \frac{1}{N} \sum_{k=1}^{N} J_1(c - (k-1)\beta_2 z_A)$. Without in-line compensation, the span contributions $J_1(c - (k-1)\beta_2 z_A)$ are non-overlapping and thus we very simply have

$$\int_{-\infty}^{\infty} J^2(c) \frac{dc}{2\pi} = \frac{1}{N^2} \sum_{k=1}^{N} \int_{-\infty}^{\infty} J_1^2(c - (k-1)\beta_2 z_A) \frac{dc}{2\pi} = \frac{1}{N} \int_{-\infty}^{\infty} J_1^2(c) \frac{dc}{2\pi}.$$

Hence substitution in Eq. (23) yields

$$I_\infty = N \frac{\mathscr{K}_1(0)^2}{2} \int_{-\infty}^{\infty} J_1^2(c) \frac{dc}{2\pi} \equiv N \int_0^\infty |\mathscr{K}_1(v)|^2 dv. \tag{24}$$

For end-span lumped amplification we have $\mathscr{K}_1(0) = \gamma \frac{1 - e^{-\alpha z_A}}{\alpha}$ and ([11]):

$$J_1(c) = \begin{cases} \dfrac{e^{\alpha \frac{c}{\beta_2}}}{(1 - e^{-\alpha z_A})} \dfrac{\alpha}{|\beta_2|} & \text{for} \begin{cases} 0 < c < -z_A\beta_2 & \text{if } \beta_2 < 0 \\ -z_A\beta_2 < c < 0 & \text{if } \beta_2 > 0 \end{cases} \\ 0 & \text{else} \end{cases}$$

hence finally

$$I_\infty = N \frac{(\frac{\gamma}{\alpha})^2 (1 - e^{-\alpha z_A})^2}{2} \left[\frac{\alpha}{4\pi|\beta_2|} \frac{1 - e^{-2\alpha z_A}}{(1 - e^{-\alpha z_A})^2} \right] = N \frac{\gamma^2}{8\pi} \frac{1 - e^{-2\alpha z_A}}{\alpha|\beta_2|}. \tag{25}$$